Synthesis of Vortex Rossby Waves. Part II: Vortex Motion and Waves in the Outer Waveguide

ISRAEL GONZALEZ III

Department of Earth and Environment, Florida International University, Miami, Florida

AMARYLLIS COTTO

National Weather Service, WFO, San Juan, Puerto Rico

HUGH E. WILLOUGHBY

Department of Earth and Environment, Florida International University, Miami, Florida

ABSTRACT

Beta, the meridional gradient of planetary vorticity, causes tropical cyclones to propagate poleward and westward at approximately $2\,\mathrm{m\,s^{-1}}$. In a previous shallow-water linear model, the simulated vortex accelerated without limit, ostensibly because beta forced a free linear mode. In the analogous nonlinear model, wave–wave interaction limited the propagation speed. Subsequent work based upon the asymmetric balance (AB) approximation was unable to replicate the linear result.

The present barotropic nondivergent model replicates the linear beta gyres as a streamfunction dipole with a uniform southeasterly ventilation flow across the vortex. The simulated storm accelerates to unphysical, but finite, speeds that are limited by vorticity filamentation. In the analogous nonlinear model, nonlinearly forced wavenumber-1 gyres have opposite phase to the linear gyres so that their ventilation flow counteracts advection by the linear gyres to limit the overall vortex speed to approximately $3\,\mathrm{m\,s^{-1}}$.

A bounded mean vortex with zero circulation at large radius must contain an outer annulus of anticyclonic vorticity to satisfy the circulation theorem. The resulting positive mean vorticity gradient constitutes an outer waveguide that supports downstream-propagating, very-low-frequency vortex Rossby waves. It is confined between an inner critical radius where the waves are absorbed and an outer turning point where they are reflected. Vorticity filamentation at the critical radius limits the beta-drift acceleration. The original unlimited linear acceleration stemmed from too-weak dissipation caused by second-order diffusion applied to velocity components instead of vorticity. Fourth-order diffusion and no outer waveguide in the Rankine-like vortex of the AB simulations plausibly explain the different results.

1. Introduction

Tropical cyclone (TC) track forecasting has improved substantially since the mid-twentieth century, largely through improved physical understanding. In simplest terms, TC motion can be thought of as the vector sum of advection by the surrounding wind and propagation, primarily due to beta β, the meridional gradient of the Coriolis parameter f (Holland 1983). In the Northern Hemisphere, β forces a wavenumber-1 asymmetry composed of a cyclonic gyre southwest of the center and an anticyclonic gyre northeast of it, such that the flow between these "β gyres" advects the vortex poleward and westward. During the 1980s and 1990s, β-gyre dynamics was the focus of intense modeling and observational efforts (e.g., Chan and Williams 1987; Chan 2005; Li and Wang 1994; Ritchie and Frank 2007).

Willoughby (1992, hereafter W92, and 1994, hereafter W94) used linear and nonlinear versions of a primitive-equation, vortex-tracking semispectral model to simulate the motion of a shallow-water barotropic vortex on a β plane. In the linear model, the vortex accelerated toward the northwest without limit, ostensibly through

Corresponding author address: Hugh E. Willoughby, Department of Earth and Environment, Florida International University, 11200 SW 8th Street, AHC-5 360, Miami, FL 33199.
E-mail: hugh.willoughby@fiu.edu

resonant growth of a free linear mode. In the analogous nonlinear model, wave–wave interaction limited the westward and poleward motion to reasonable speeds of a few meters per second. Subsequent work by Montgomery et al. (1999, hereafter MMN) was unable to replicate the linear acceleration. Here, building upon Gonzalez (2014), we revisit the problem using a different mean vortex in a barotropic nondivergent (BND) context both to resolve the question of the free mode's existence and to clarify the nonlinear dynamics. Since the BND model is the simplest one possible that contains the essential rotational dynamics of vortex motion on a β plane, the results clarify the mechanism of TC motion and its sensitivity to dissipation and mean wind profile.

2. Rotational dynamics

In idealized TCs, the winds swirl cyclonically around the center, for the most part in gradient balance with almost circular pressure fields (Fig. 1a). Since TC dynamics are overwhelmingly rotational, absolute vorticity conservation is a conceptually simple basis for modeling them in the BND context. The BND absolute vorticity is the sum of relative and planetary vorticities. Beta, $\beta = \partial f / \partial y$, represents the change in f across the circulation. The axially symmetric relative vorticity decreases outward in a neighborhood around TCs' centers. In vortices with nonzero circulation at large radius, the vorticity decrease can be monotonic. In bounded vortices, such that the circulation becomes zero beyond some finite radius, an outer annulus of anticyclonic relative vorticity exists, consistent with the circulation theorem (Fig. 1b). This feature supports a positive (more negative to less negative) peripheral vorticity gradient. Thus, bounded and unbounded (i.e., monopole) vortices can have significantly different vortex Rossby wave (VRW) propagation.

Vorticity is a conservative property in frictionless BND flows; although in nature it is stretched, compressed, and tilted. Diabatically-induced updrafts sustain the axially symmetric primary vortices of real TCs through vorticity tilting and stretching. In the BND model the vortex wind and vorticity profiles are specified at the outset and maintained throughout the calculation.

Conservation of absolute vorticity should require equatorward-moving air parcels to develop cyclonic relative vorticity as they encounter less cyclonic planetary vorticity; whereas poleward-moving parcels develop anticyclonic relative vorticity as they encounter more cyclonic planetary vorticity. By itself, conservation of absolute vorticity would induce a cyclonic relative vorticity gyre equatorward of the vortex center and an
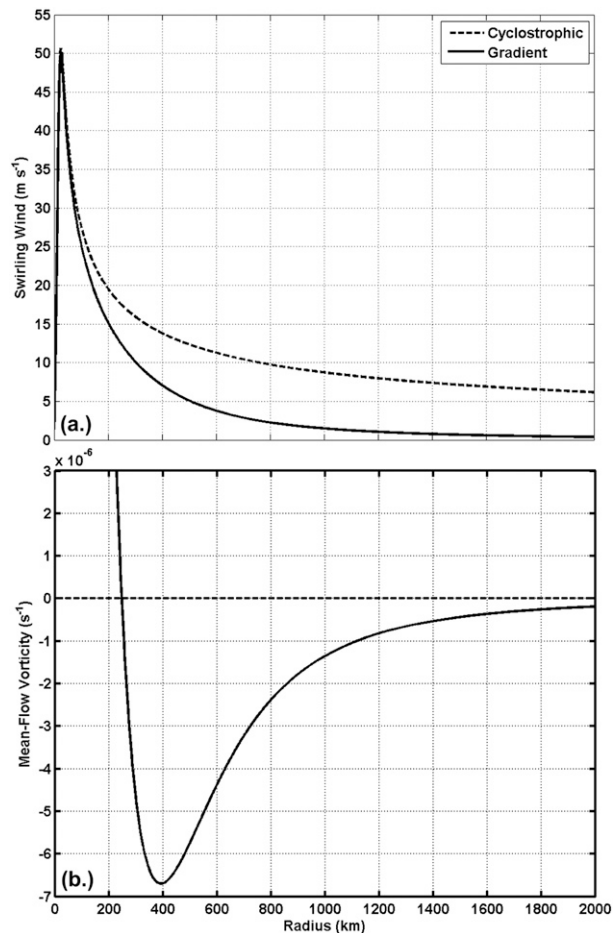

FIG. 1. (a) Cyclostophic and gradient swirling wind from the WW11 mean vortex and (b) corresponding relative vorticity scaled to emphasize the outer waveguide.

anticyclonic gyre poleward of it. More generally, nonzero radial gradients of axially symmetric relative vorticity exist. Radial advection, time changes, and the vortex motion through its surroundings also contribute to the process (e.g., Chan and Williams 1987). These factors change the phase and amplitude of the induced β gyres.

Gradients of mean-flow vorticity can also support propagation of VRWs (e.g., MacDonald 1968; Montgomery and Kallenbach 1997), but they are zero outside the cores of Rankine-like, unbounded vortices where cyclonic vorticity concentrated in the vortex core induces a free (i.e., irrotational) circulation that extends to large radius. It is generally accepted that some combination of these processes (e.g., Holland 1984) and not a net Coriolis force (Rossby 1948) acting on the vortex is responsible for the approximately $2\,\mathrm{m\,s}^{-1}$ poleward and westward "β drift" superimposed on advection by surrounding "steering currents."

W92 and W94 developed a shallow-water (500-m depth) time-marching model to simulate both linear and nonlinear vortex motion. It had 4-km horizontal resolution on a 3000-km domain. The vortex was bounded at 1000-km radius with zero circulation beyond that radius so that the cyclonic core was surrounded by anticyclonic vorticity and a reversal of vorticity gradient.

The linear case produced a β-gyre streamfunction dipole that appeared to represent a normal mode because it grew linearly with time to large amplitude when beta forced it at zero frequency, and it was able to persist in the absence of explicit forcing when beta was turned off after the asymmetry had developed for 240 h. The track from linear calculations showed an essentially constant acceleration poleward and westward to unphysically high speeds. It was possible by rotating and scaling the β gyres to reinitialize vortex motion with any desired speed or direction.

In the analogous nonlinear case, wave–wave interactions changed the axially symmetric structure of the vortex, produced destructive interference among the Fourier components, and limited propagation speed. The nonlinear evolution of the mean vortex produced an annulus of anticyclonic flow on the vortex periphery that forced a set of outer β gyres of opposite polarity to the original inner ones.

Asymmetric balance (AB; Montgomery and Shapiro 1992) can support simulation of quasi-balanced flows' contribution to the vortex motion even when the Rossby number is large (i.e., $V_0/fL \gg 1$, where V_0 is the mean swirling velocity and L is the characteristic horizontal dimension). The AB approximation requires the linearized Doppler-shifted frequencies to be well below the local inertia frequency. AB was designed to be a mathematical framework for studying the slow evolution of rapidly rotating fluid systems such as TCs. It can address asymmetric dynamics of phenomena such as spiral rainbands, vortex motion, and TC–environment interaction.

MMN's AB simulation of shallow-water vortex motion yielded different linear results from W92 inasmuch as their translation speed asymptotically approached approximately $6\,\mathrm{m\,s^{-1}}$ after 240 h. The speed was faster than full-physics models or observations and not much slower than W92's linear $8\,\mathrm{m\,s^{-1}}$. Possible reasons for the different results include use of different vortex tracking, significantly different vorticity dynamics in MMN's completely cyclonic vortex, or fourth-order ($K = 60\,\mathrm{m^2\,s^{-1}}$) instead of second-order diffusion. MMN argued against existence of β-gyre normal modes because finite drift speeds were always attained with the AB approximation in a finite-depth vortex. In AB reinitialization experiments, the β gyres persisted for long times but not indefinitely. They decayed and "axisymmetrized" with a half-life proportional to the radial shear.

3. Vortex Rossby waves

Here we continue the VRW work of Cotto (2012), Gonzalez (2014), and Cotto et al. (2015, hereafter Part I) by applying linear and nonlinear versions of the same formulation to wavenumber-1 waves on a BND vortex that moves through a still environment on a β plane. Where the mean vorticity decreases outward, VRWs propagate upstream so that their azimuthal phase velocity with respect to the ground is slower than the mean swirling flow. Thus, they are advected cyclonically downstream. As described in Part I, two-dimensional BND Rossby waves in cylindrical coordinates are confined to a "passband" between zero frequency and Ω_{1D}, the frequency of a one-dimensional Rossby wave with the same tangential wavenumber and rotation frequency. The latter frequency marks a turning point where the local radial wavenumber passes through zero so that the radial structures of VRWs on the high-frequency side of the turning-point radius are evanescent rather than sinusoidal.

This work revisits W92 and W94's vortex-following, shallow-water, β-plane modeling, but in a BND context. The model is completely reformulated in MATLAB. It is initialized from asymmetry and rest. Time integration of the vorticity equation yields the asymmetric structure of the vortex, including a well-defined wavenumber-1 asymmetry resulting from the displacement between the center of mean-vortex rotation and the origin of the cylindrical coordinates. After each time step, the vortex is repositioned to remove the apparent asymmetry, and the motion inherited from previous computations is updated. This is the simplest model that embodies the essential rotational dynamics of the β drift.

Translating cylindrical coordinates (Fig. 2) are the natural choice to represent the moving circular mean vortex. The variables used are mean tangential wind V_0; radius r; azimuth angle reckoned cyclonically from north λ; wavenumber-1, perturbation radial wind component u_1 (positive outward); perturbation tangential wind component v_1 (positive cyclonically); perturbation geopotential ϕ_1; Coriolis parameter at the vortex center (nominally at 20°N; assumed constant) f_0; and β (also assumed constant).

The derivation of the BND vorticity equation begins with the linearized radial and tangential momentum equations [(1a) and (1b)], where $\partial/\partial t + (V_0/r)\partial/\partial \lambda$ represents the linearized Lagrangian derivative, $\xi_0 = 2V_0/r + f_0$ is the inertial parameter, $\zeta_0 = \partial V_0/\partial r + V_0/r + f_0$ is the mean-flow vorticity, and c_r and c_λ are, respectively, the radial and tangential components of the reference-frame motion:
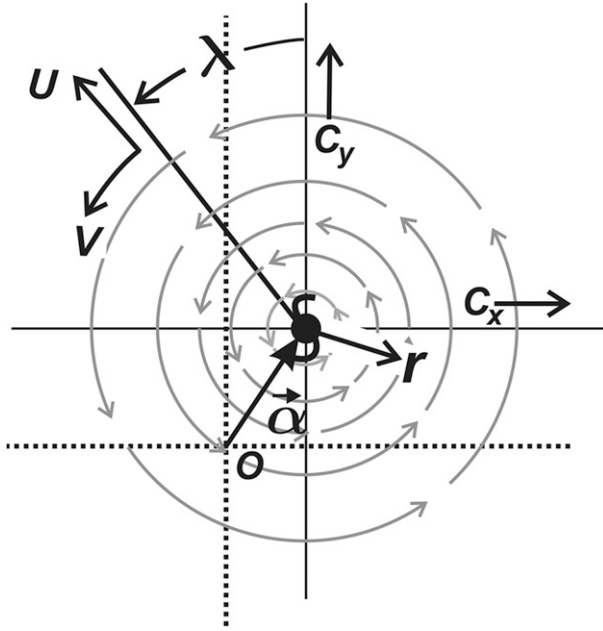
FIG. 2. Translating cylindrical coordinates, illustrating the mean swirling flow, perturbation velocity components, vortex translation, and centering error. The hurricane symbol indicates the axis of vortex rotation displaced by vector $\boldsymbol{\alpha}$ from the reference-frame origin.

$$\frac{\partial u_1}{\partial t} + \frac{V_0}{r}\frac{\partial u_1}{\partial \lambda} - \xi_0(v_1 - c_\lambda) + \frac{\partial \phi_1}{\partial r} = \beta r V_0 \cos\lambda \quad \text{and}$$

$$(1a)$$

$$\frac{\partial v_1}{\partial t} + \frac{V_0}{r}\frac{\partial v_1}{\partial \lambda} + \zeta_0(u_1 - c_r) + \frac{1}{r}\frac{\partial \phi_1}{\partial \lambda} = 0. \quad (1b)$$

Cross-differentiating and eliminating the geopotential yields the vorticity equation:

$$\left(\frac{\partial}{\partial t} + \frac{V_0}{r}\frac{\partial}{\partial \lambda}\right)\left(\frac{\partial v_1}{\partial r} + \frac{v_1}{r} - \frac{1}{r}\frac{\partial u_1}{\partial \lambda}\right) + \zeta_0\left(\frac{\partial u_1}{\partial r} + \frac{u_1}{r} + \frac{1}{r}\frac{\partial v_1}{\partial \lambda}\right)$$

$$+ (u_1 - c_r)\frac{\partial \zeta_0}{\partial r} = \beta V_0 \sin\lambda. \quad (2)$$

Nondivergence means that the second term in (2) is zero and that u_1 and v_1 can be represented with a streamfunction, $\psi_1(r, \lambda, t)$, such that $u_1 = -(1/r)\partial\psi_1/\partial\lambda$, $v_1 = \partial\psi_1/\partial r$, and $\zeta_1 = \partial v_1/\partial r + v_1/r - r^{-1}\partial u_1/\partial\lambda = \partial^2\psi_1/\partial r^2 + r^{-1}\partial\psi_1/\partial r + r^{-2}\partial^2\psi_1/\partial\lambda^2$. Thus, (2) becomes

$$\left(\frac{\partial}{\partial t} + \frac{V_0}{r}\frac{\partial}{\partial \lambda}\right)\left(\frac{\partial^2\psi_1}{\partial r^2} + \frac{1}{r}\frac{\partial\psi_1}{\partial r} + \frac{1}{r^2}\frac{\partial^2\psi_1}{\partial\lambda^2}\right)$$

$$- \left(\frac{1}{r}\frac{\partial\psi_1}{\partial\lambda} + c_r\right)\frac{\partial\zeta_0}{\partial r} = \beta V_0 \sin\lambda. \quad (3)$$

We seek time-domain solutions for the wavenumber-1 streamfunction. We assume that the solutions are products

of imaginary exponents in azimuth with a complex amplitude that is a function of radius and time, $\psi_1(r, \lambda, t) = \text{Re}[\Psi_1(r, t)e^{-i\lambda}]$. To facilitate discussion, we sometimes treat these solutions as though the time variation could be represented with a nonzero rotation frequency ω. In the time domain, the vorticity equation becomes a second-order radial-structure equation for the streamfunction amplitude:

$$\left[\frac{\partial}{\partial t} - \frac{iV_0(r)}{r}\right]\left(\frac{\partial^2\Psi_1}{\partial r^2} + \frac{1}{r}\frac{\partial\Psi_1}{\partial r} - \frac{\Psi_1}{r^2}\right)$$

$$+ \left(\frac{i\Psi_1}{r} - c_r\right)\frac{\partial\zeta_0(r)}{\partial r} = i\beta V_0. \quad (4)$$

In the beta-plane problem, $\omega = 0$ because the β forcing is steady. The complex representation of the radial reference frame's motion is $c_r = \text{Re}[-i(c_x + ic_y)e^{-i\lambda}]$, consistent with W92. If one replaces the time derivative with a specified rotation frequency for the wave train, $\partial/\partial t \rightarrow i\omega$, such that the leading factor that multiplies the vorticity in (4) is the Doppler-shifted frequency, $i\Omega = i(\omega - V_0/r)$. Even though ω is constant, the Doppler-shifted frequency is a variable function of r. As in Part I, assuming zero-order, Hankel-function local solutions produce a local dispersion relation:

$$\Omega = \left(\omega - \frac{V_0}{r}\right) = \frac{(1/r)(\partial\zeta_0/\partial r)}{k_r^2 + (1/r^2)}, \quad (5)$$

where k_r is the local radial wavenumber. As with planetary Rossby waves, Ω is negative when $\partial\zeta_0/\partial r < 0$. Since V_0 decreases as r increases, $-V_0/r$ becomes smaller (less negative) away from the center and larger (more negative) toward the center. At the critical radius where Ω approaches zero, the waves become locally very short and are absorbed. When $\partial\zeta_0/\partial r > 0$ far from the center in bounded vortices, the VRWs propagate downstream so that the critical radius is nearer the center.

Examination of (5) shows that radial group and phase velocities are of opposite sign and can be inward or outward. The limits of wave propagation speed are dictated by k_r. The most negative $\Omega = \Omega_{1D} \equiv (\partial\zeta_0/\partial r)(n/r)^{-1}$ coincides with a turning point of (5) where k_r is locally zero and (5) reduces locally to the dispersion relation for a one-dimensional VRW. It also corresponds to the fastest tangential wave propagation with respect to the mean wind (the most negative possible value of Ω at any radius). At Ω_{1D}, the group velocity is zero. For small positive or negative radial wavenumbers, the group velocities are slow and of opposite sign to the wavenumber. For frequencies greater than Ω_{1D}, the radial wavenumber is imaginary so that the solutions are radially evanescent. Thus, VRWs are at least partially reflected because they can jump to the

solution with opposite radial group velocity in the neighborhood of the turning point when their frequencies are Doppler shifted to Ω_{1D}. This process is simplest when the domain extends far on the high-frequency side of the turning-point radius. If the situation is complicated by nearby domain boundaries or additional turning points that restore sinusoidal propagation, varying degrees of partial reflection or overreflection are possible. The latter possibility offers an interesting perspective on instability (e.g., Lindzen and Tung 1978; Lindzen and Baker 1985) in other contexts.

In contrast with Part I, here we seek time-domain solutions. The model integrates the system defined by (4), retaining the time-domain derivative of vorticity as a second-order finite difference, to march the wavenumber-1 vorticity forward in time. Once the vorticity has been advanced to the new time level, the model uses the Lindzen and Kuo (1969; see also Part I) algorithm to invert the Poisson equation for the streamfunction. Solutions are semispectral with sinusoidal variation (wavenumber 1 only) in azimuth and finite-difference representation in azimuth and time. The domain extends to 4000-km radius with uniform 1-km resolution. In addition, the outer 500 km of the domain contains a ''sponge ring'' that, as the name suggests, absorbs waves through imposed strong Newtonian dissipation. As a result, any outward-propagating waves that approached the outer boundary would be absorbed so that the physical solutions would not be contaminated by reflection.

During each time step, the model retains the vortex motion inherited from the previous iteration. Since the vortex is generally accelerating, the computed streamfunction also contains an ''α gyre'' (pseudo mode) component, complex representation $i(\alpha_x + i\alpha_y)V_0(r)$. The α gyres are apparent asymmetries that arise from misalignment between the predicted center of rotation of the mean vortex and the coordinates' origin. The α-gyre streamfunction is proportional to the misalignment vector and mean swirling wind profile. Thus, a complex least squares fit of $V_0(r)$ to $\Psi_1(r, t)$ provides a good approximation to the center-positioning error and the α-gyre asymmetry. Since the CFL criterion is much less of an issue in the BND model than it was in the primitive-equation model of W92, the present model repositions the vortex after each of its relatively long time steps.

This vortex-tracking method differs significantly from MMN's AB model, which was set in fixed coordinates that were periodically repositioned to move the vortex center to the center of a circle fitted to the height contour at the radius of maximum wind. As shown subsequently, the consistency between the current results and MMN's argues against different centering as an explanation for the different AB results.

4. Linear results

The linear model obtains solutions for the vorticity, streamfunction, and motion forced directly through advection of β by the mean swirling flow. The axially symmetric swirling flow advects planetary and perturbation vorticity. The asymmetric perturbation radial flow advects axially symmetric mean vorticity. The model is initialized from zero perturbation amplitude and rest, marches the vorticity forward in 2.5-min (150 s) time steps, and utilizes the Lindzen–Kuo solver to invert the vorticity to obtain the streamfunction and adjusts the vortex position. The new vorticity then becomes the input for the next time step.

The mean cyclostrophic wind (Fig. 1a) follows the same Wood and White (2011, hereafter WW11) profile used in Part I, with specified maximum tangential wind ($V_{MAX} = 50\,m\,s^{-1}$), radius of maximum wind (RMW; 25 km), and three parameters that define the power-law exponent's shape inside the eye (proportional to between r and $r^{3/2}$), power-law shape outside the eye (proportional to $r^{-1/2}$), and the width of the transition between these power laws in the neighborhood of the RMW. Thus, the cyclostrophic circulation would be unbounded in the sense that its circulation becomes arbitrarily large with increasing radius. The model, however, uses the gradient wind computed from the cyclostrophic wind (e.g., Willoughby 2011). Its circulation decreases with increasing radius so that the mean vortex is bounded in the limit of large radius. As shown previously, the outer part of the vortex contains a ring of anticyclonic relative vorticity (Fig. 1b) and a positive radial vorticity gradient. In bounded vortices, such as the gradient-balance WW11 profile, the beta gyres may be VRWs propagating downstream on the reversed peripheral-mean vorticity gradient. They would be confined to a frequency band between zero and (a now positive) Ω_{1D}. Thus, in bounded vortices there is a potential for two waveguides to exist. The inner guide supports propagation against the cyclonic mean flow, while the outer has the waves that propagate faster than the mean flow. Since both the mean swirling flow and the vorticity gradient are weak in the outer waveguide, the VRW propagation should be slow.

For comparison, we also simulate motion using the mean vortex of MMN. It is essentially a smoothed Rankine vortex with all of its vorticity concentrated in the core, a narrow skirt of cyclonic vorticity extending a short distance beyond the RMW, and an extensive free vortex that has constant circulation extending to arbitrarily large radius (Fig. 3a). As described previously, the gradient WW11 vortex has an outer waveguide for downstream-propagating VRWs. Since the MMN
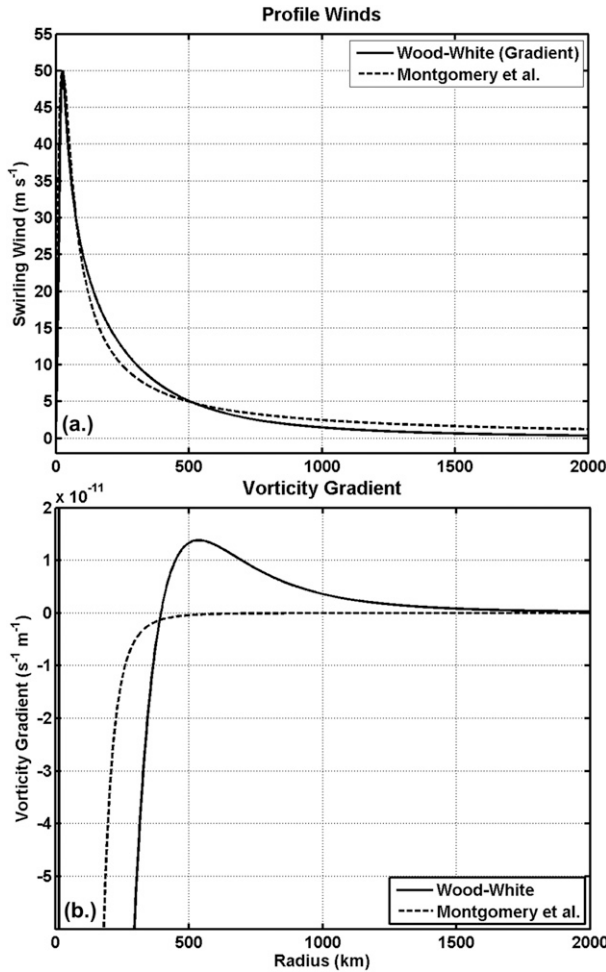
FIG. 3. Radial profiles of (a) wind and (b) vorticity gradient, comparing the gradient wind WW11 profile (solid) with that used in MMN (dashed).

vortex has a monotonic negative vorticity gradient, it has no outer waveguide (Fig. 3b).

Since this is a time-marching problem, (4) is solved for the perturbation vorticity tendency:

$$\frac{\partial \zeta_1}{\partial t} = -\frac{V_0}{r}\frac{\partial \zeta_1}{\partial \lambda} - (u_1 - c_r)\frac{\partial \zeta_0}{\partial r} + \beta V_0 \sin\lambda. \quad (6)$$

The terms on the right-hand side are perturbation vorticity advection by the mean tangential wind, mean-flow vorticity advection by both the radial perturbation flow and the vortex motion, and planetary vorticity-gradient advection by the mean flow. The numerical algorithm uses leapfrog time marching with an Asselin filter. The model typically runs for 10 simulated days (240 h or 2880 time steps).

The complete linear solution replicates the results of W92 with a northwestward track that accelerates throughout the simulation but may asymptote after 240 h. The vortex moves a total of approximately 5400 km in 10
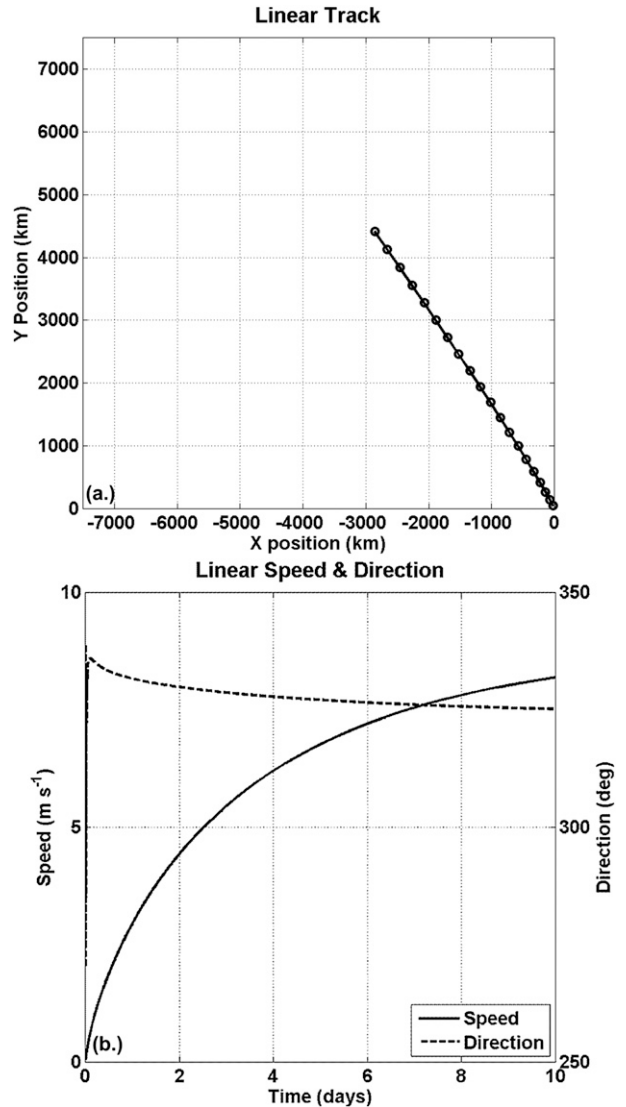

FIG. 4. (a) Track and (b) speed and direction of motion for the WW11 vortex initialized from rest and axial symmetry on a β plane at 20°N latitude.

simulated days (Fig. 4a) with an average speed of about 6.25 m s^{-1} and final speed of 8.5 m s^{-1} (Fig. 4b). The large distance traveled by the vortex in this model compared with approximately 3800 km in W92 stems from a larger vortex, nondivergence, and weaker dissipation. Since the Poisson equation for the vorticity does not contain the Rossby-radius term, it yields a larger streamfunction than the divergent model would with the same vorticity. The mean vortex translation was toward 325°. The speed is sensitive to the imposed diffusion with $K = 1 \, \text{m}^2 \, \text{s}^{-1}$. Larger values yield slower acceleration.

The vorticity field exhibits trailing spirals that become filamented at the critical radius, 500–700 km (Fig. 5a). The vorticity filaments wrap tightly around the vortex
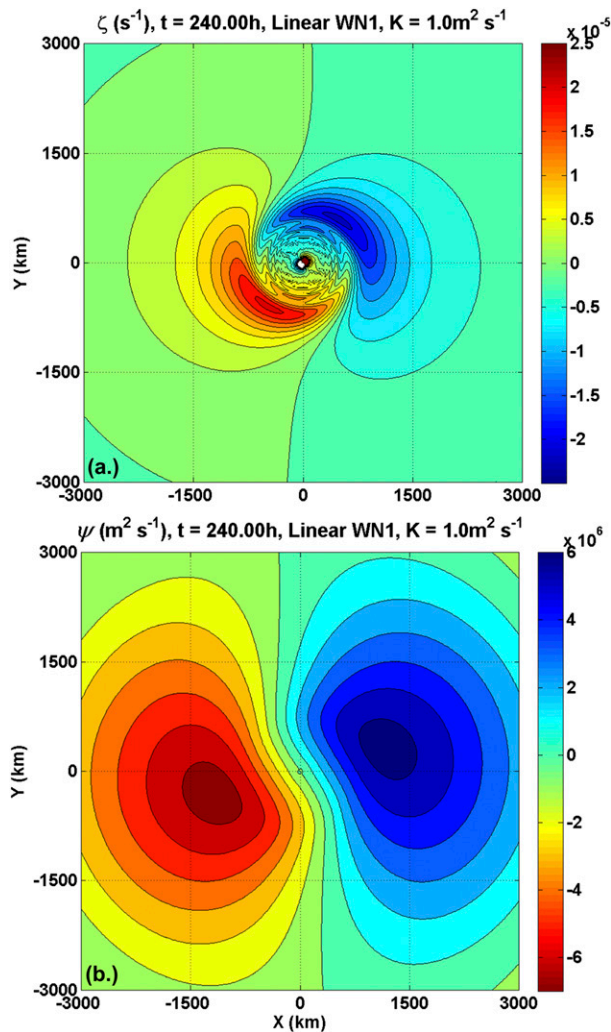
FIG. 5. (a) Wavenumber-1 vorticity and (b) streamfunction for the WW11 vortex moving on a β plane, as shown in Fig. 4.
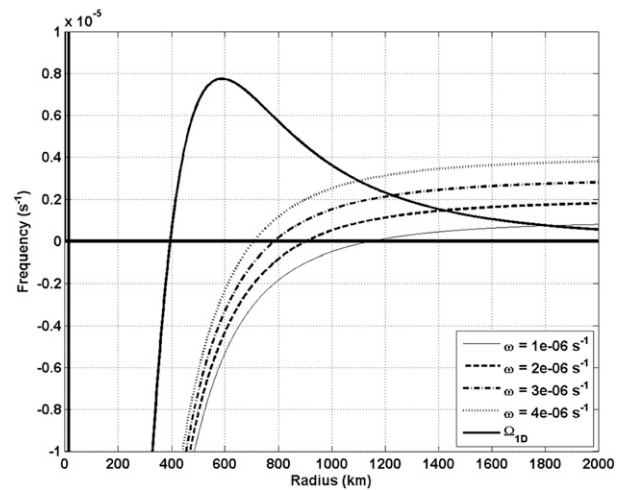

FIG. 6. Radial variation of Doppler-shifted frequency on the periphery of the WW11 vortex for different very low values of the rotation frequency with respect to the ground ω. The outer waveguide lies between zero Doppler-shifted frequency and Ω_{1D}.

near this radius, where their frequencies are Doppler-shifted to zero. Vorticity waves' inward-propagating energy is absorbed at the critical radius as their radial wavelengths become increasingly shorter. Conversely, the frequencies of waves that propagate outward are Doppler shifted to Ω_{1D} so that they are at least partially reflected, typically at $r > 1000$ km. The streamfunction field illustrates the β gyres as a dipole in the outer part of the vortex (Fig. 5b). For simplicity, we adopt a consistent color table where cool colors represent anticyclonic vorticity and streamfunction, $\zeta < 0$ and $\psi > 0$, and warm colors represent cyclonic vorticity and streamfunction, $\zeta > 0$ and $\psi < 0$. Contours of ψ represent streamlines of the perturbation flow. The streamfunction amplitude is proportional to the vortex speed and the contour lines' direction across the center is consistent with northwestward translation.

The radial variation of the β gyres' Doppler-shifted frequency in the linear model is subtle. Although the forcing is exactly at zero frequency, it also excites waves with nonzero, but very low, frequencies that are nearly in resonance. VRWs in the outer waveguide have nearly zero cyclonic frequencies. They can propagate with a small radial group velocity in a narrow passband between zero frequency and Ω_{1D} (Fig. 6). The densely packed set of low-frequency waves in the outer waveguide makes up another example of the quasimode-like feature (Schecter et al. 2000; Schecter and Montgomery 2003, 2004) described in Part I. Beta forces these waves close to their resonance, allowing them to grow linearly to large amplitude given sufficient time. This process appears to explain the continuing acceleration in the original linear model. The largest-amplitude ($\omega = 1 \times 10^{-6}\,\mathrm{s}^{-1}$) wave is confined to a radial interval between 1100 and 1700 km, which includes the centers of the β gyres.

Loss of energy propagating to the critical radius causes the VRWs to be weakly damped so that the waveguide in which they are trapped is "leaky" in the sense that wave energy is lost through critical-radius absorption. Initially inward-propagating energy eventually reaches the critical radius where its vorticity becomes filamented and is transferred to the mean flow. Initially outward-propagating energy is at least partially reflected at the turning-point radius and then propagates inward to be absorbed at the critical radius. Since the Doppler-shifted frequencies are so low, the radial group velocities are slow and dissipation by this process is gradual. Whether the VRWs represent a continuum or a cluster of discrete frequencies is unclear; although the former interpretation seems more likely.

5. Nonlinear model

The nonlinear version of the model represents only semispectral interactions between waves with azimuthal wavenumbers 1 and 2 so that the streamfunction is $\Psi_1(r, t)e^{-i\lambda} + \Psi_2(r, t)e^{-2i\lambda}$. Fourier transformation in azimuth simplifies the system to two linear vorticity equations. Wave–wave interaction terms couple the equation and contain all of the nonlinearity. Linearly forced (by β) wavenumber 1 interacts nonlinearly with itself to force wavenumber 2, while wavenumber 1 interacts nonlinearly with wavenumber 2 to force the nonlinear part of wavenumber 1.

This formulation calculates the complex wavenumber-1 and -2 vorticities in the same way as the linear model but with a subset of the possible nonlinear interactions included. We separate the solutions into three vorticity and stream-function components: linearly forced wavenumber 1, non-linearly forced wavenumber 2, and nonlinearly forced wavenumber 1. Computation of linear wavenumber-1 vorticity is analogous with the linear model, apart from the effect of slower motion. The significant differences lie in wavenumber 2 and nonlinear wavenumber 1.

The algorithm is a much simplified version of that used in W94. Time marching the complex wavenumber-2 vorticity equation advances the vorticity forced by nonlinear interactions of wavenumber 1 with itself:

$$\frac{\partial \zeta_2}{\partial t} = -\frac{v_0}{r}\frac{\partial \zeta_2}{\partial \lambda} - u_2 \frac{\partial \zeta_0}{\partial r} - (v_1 - c_\lambda)\left(\frac{1}{r}\frac{\partial \zeta_1}{\partial \lambda} - \beta \sin\lambda\right)$$
$$- (u_1 - c_r)\left(\frac{\partial \zeta_1}{\partial r} + \beta \cos\lambda\right). \quad (7)$$

The terms on the right-hand side are linear tangential vorticity advection by the mean vortex, linear radial advection of mean-vorticity by the perturbation flow, and nonlinear tangential and radial advection of perturbation and planetary vorticity. The nonlinear tendency equation for the wavenumber-1 complex vorticity is nearly the same as (7), but with additional terms representing the forcing (from β effect and vortex motion):

$$\frac{\partial \zeta_1}{\partial t} = -\frac{v_0}{r}\frac{\partial \zeta_1}{\partial \lambda} - (u_1 - c_r)\frac{\partial \zeta_0}{\partial r} + \beta v_0 \sin\lambda$$
$$- (\overline{v_1 - c_\lambda})\frac{1}{r}\frac{\partial \zeta_2}{\partial \lambda} - v_2\left(\frac{1}{r}\frac{\overline{\partial \zeta_1}}{\partial \lambda} - \beta \sin\lambda\right)$$
$$- (\overline{u_1 - c_r})\frac{\partial \zeta_2}{\partial r} - u_2\left(\frac{\overline{\partial \zeta_1}}{\partial r} + \beta \cos\lambda\right). \quad (8)$$

Overbars denote complex conjugates. The model marches (7) and (8) forward in time, inverts Poisson equations forced by the resulting vorticities to obtain wavenumber-1
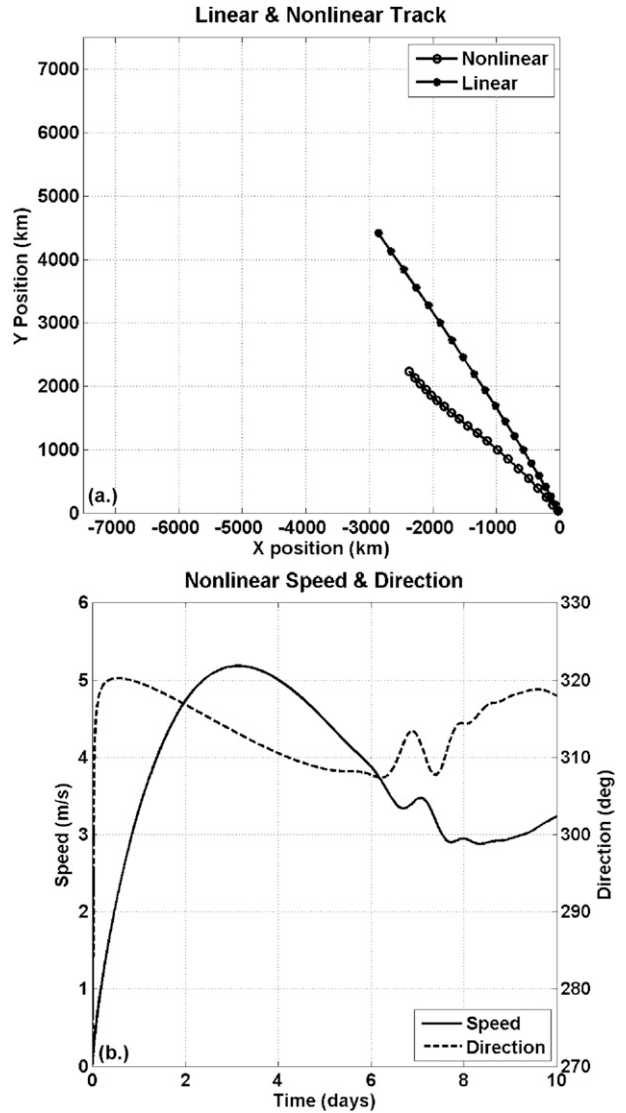

FIG. 7. (a) Track of a WW11 vortex moving nonlinearly for 240 h with truncation at tangential wavenumber 2 on a β plane, and (b) its speed and direction of motion as functions of time.

and -2 streamfunctions, and applies α-gyre closure to Ψ_1 to track the vortex motion. We artificially separate ζ_1 into a linear part forced by the terms on the right-hand side of the first line of (8) and a nonlinear part forced by the terms in the second line. Since the actual solutions are the real parts of ζ_1 and ζ_2, we neglect nonlinearly forced ζ_0 and ζ_3, as well as all other nonlinearly forced vorticities.

The nonlinear-model results replicate W94 by significantly limiting the vortex translation speed. For the entire 10-day simulation, the vortex travels only about 3260 km, equivalent to an average speed of 3.8 m s^{-1} (Fig. 7a). The motion is faster than in W94 for the same reasons as in the linear model, plus it has more severe
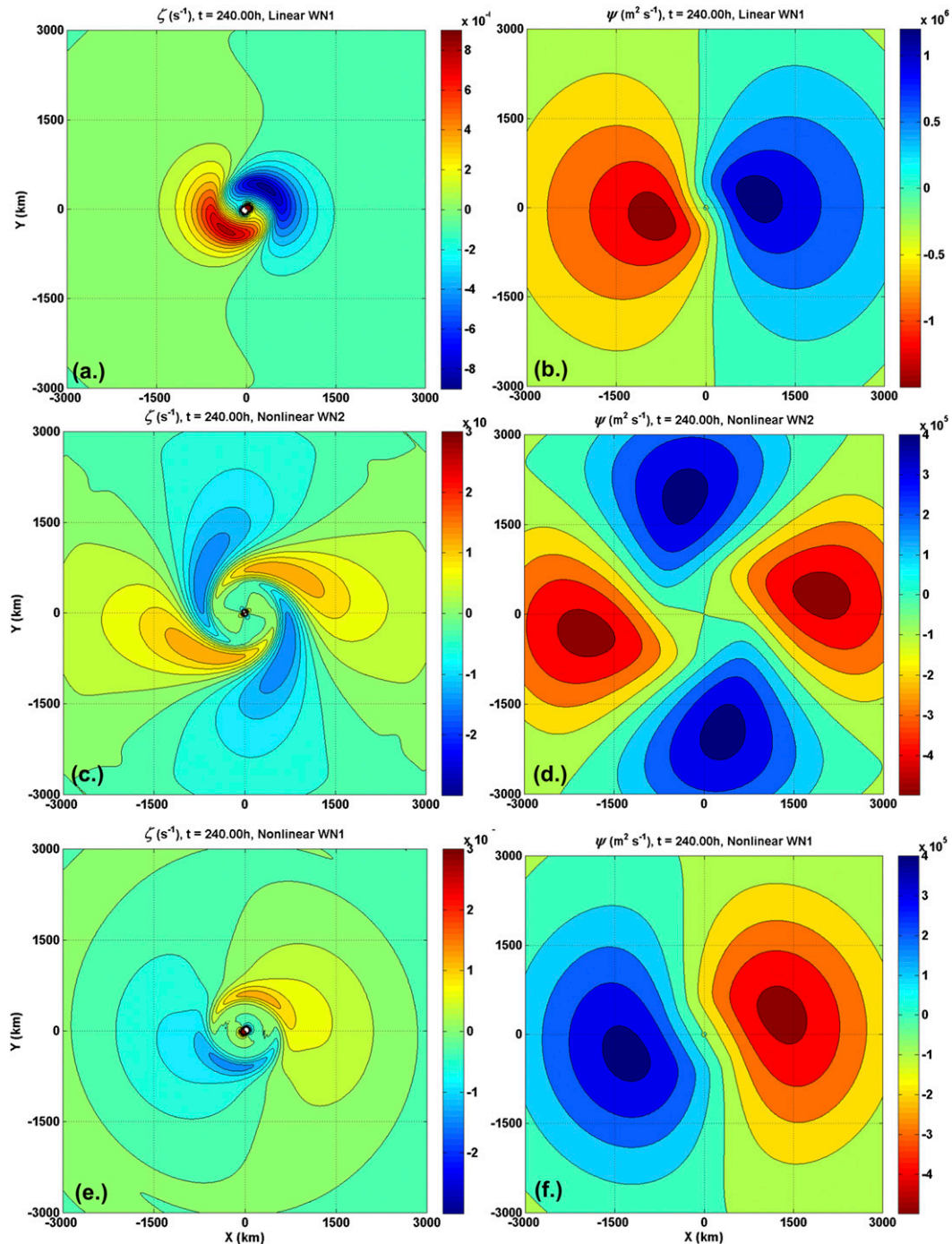
FIG. 8. Asymmetric perturbation fields for a WW11 vortex moving nonlinearly on a β plane: linearly forced wavenumber-1 (a) vorticity and (b) streamfunction, nonlinearly forced wavenumber-2 (c) vorticity and (d) streamfunction, and nonlinearly forced wavenumber-1 (e) vorticity and (f) streamfunction. The phase reversal of (e) and (f) relative to (a) and (b) illustrates the mechanism by which wave–wave interaction limits vortex speed.

spectral truncation in azimuth. The translation speed oscillates between 3 and 5 m s^{-1} because wavenumber 2 initially grows slowly and then becomes larger than is needed to control the linear acceleration. As a result, the

beta gyres decrease leading to slowing motion, followed by a weak acceleration as wavenumber 2 approaches equilibrium. These dynamics also occurred in W94 (his Fig. 1). Ultimately, the translation speed oscillates
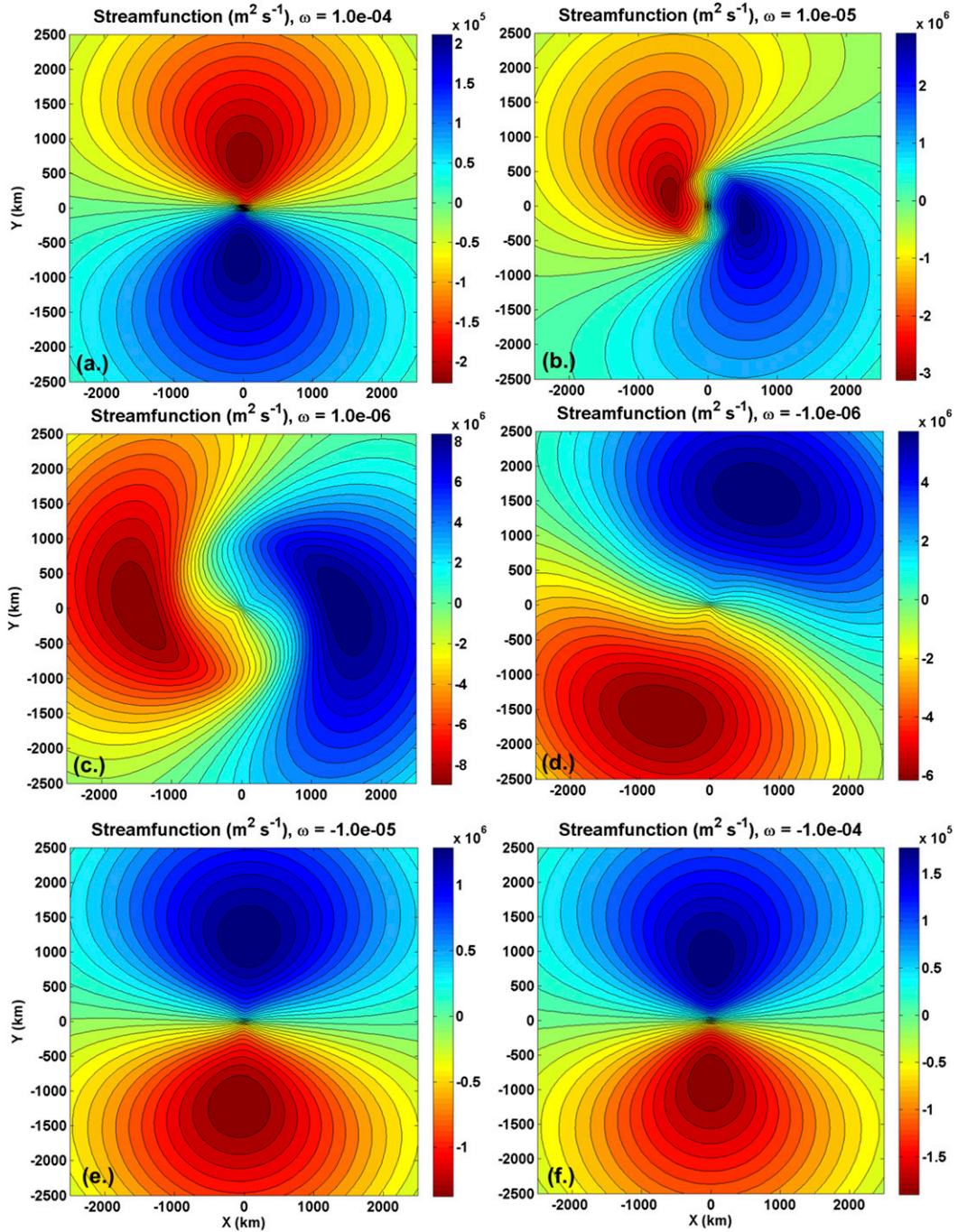
FIG. 9. Wavenumber-1 asymmetries forced by β-like forcing that rotates with frequencies (a) 1×10^{-4}, (b) 1×10^{-5}, (c) 1×10^{-6}, (d) -1×10^{-6}, (e) -1×10^{-5}, and (f) -1×10^{-4} s^{-1}. The phase reversal and maximum amplitude at $\omega = 1 \times 10^{-6}$ are consistent with nearly resonant forcing of a vortex Rossby wave trapped in the outer waveguide.

around 3 m s^{-1} near the end of the computation (Fig. 7b). The direction of motion is generally northwestward ($\sim$325°), but not as consistently as in the linear model. The computed translation speed is faster than the 2 m s^{-1} β drift observed in nature. Nonlinearly forced changes in

the mean outer circulation that can affect the motion by changing the effective radius where the β effect acts are excluded here.

The linearly forced wavenumber-1 vorticity (Fig. 8a) and streamfunction (Fig. 8b) are much the same as in the

linear case. Nonlinear interaction of wavenumber 1 with itself forces wavenumber 2. The wavenumber-2 vorticity field displays a "sunflower" pattern with four vorticity gyres of alternating polarity. Trailing spirals and filamentation are evident near the critical radius (Fig. 8c). The wavenumber-2 streamfunction (Fig. 8d) exhibits a quadropole structure of alternating polarity, similar to that described in W94. The nonlinear wavenumber-1 vorticity field is much like its linear counterpart, but with the polarity of the vorticity gyres reversed (Fig. 8e).

A key result lies in the nonlinear wavenumber-1 streamfunction (Fig. 8f) forced by the interaction between wavenumbers 1 and 2. The resulting flow is like the linear β gyres, but with the anticyclonic gyre southwest of the center and the cyclonic gyre northeast of it. The ventilation flow between the gyres is toward the southeast, opposite to the northwestward flow between the linear β gyres that is responsible for the β drift. Formation of these nonlinearly forced "anti-β gyres" constitute the mechanism that limits the vortex translation speed in the nonlinear model.

6. Frequency-domain solutions

The predecessor of the original time-domain simulation was a frequency-domain model (Willoughby 1988) that attempted to simulate steady linear motion on a β plane of a shallow-water (4-km depth) vortex. The model diagnosed the streamfunction, velocity potential, and geopotential at a specified frequency using the linear vorticity, divergence, and mass continuity equations. It computed the vortex translation variationally. The unrealistically fast poleward and westward motion predicted in the frequency domain first motivated the hypothetical excitation of a normal mode by the β effect. Significance of nonlinear processes became apparent subsequently.

Here we replicate this approach in a BND context to gain insight into the β gyres' dynamics. The frequency-domain version of linear model simulates for a single wavenumber-1 component at a specified frequency. Although the β-effect forcing is at zero frequency, the frequency-domain simulations' forcing has the same spatial structure as β but rotates with a low imposed frequency. The spatial domain is an annulus that excludes the subdomain within 250 km of the center to prevent growth of the α-gyre asymmetry. The perturbation streamfunction is set to zero at the $r = 250$-km boundary.

The governing equation is the wavenumber-1 vorticity equation Fourier transformed in both time and azimuth (e.g., Part I) and solved for specified frequency ω using the Lindzen–Kuo algorithm. The vorticity and streamfunction
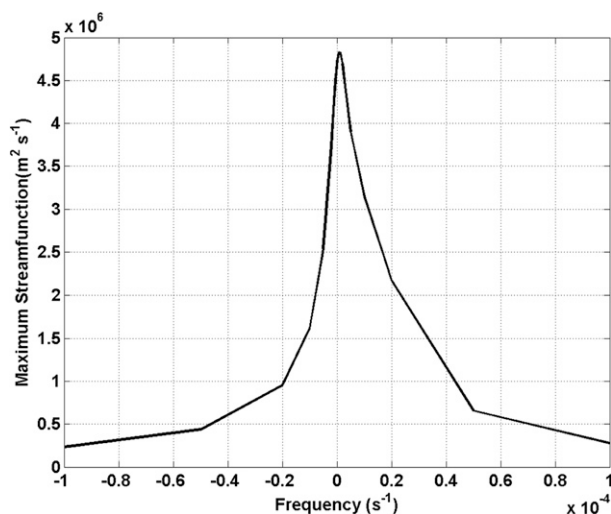

FIG. 10. Maximum streamfunction amplitude as a function of frequency for the β-plane problem illustrated in Fig. 9.

fields are aligned with the observed β gyres at near-zero frequencies but rotate from the northwest–southeast orientation for ω significantly different from zero. Frequency-domain calculations are simpler to work with. The vortex does not move, and exclusion of the domain center allows clean separation of the α and β gyres.

The streamfunction changes magnitude and rotates as the frequencies decrease by factors of 10 from 1×10^{-4} through $1 \times 10^{-6}\,\text{s}^{-1}$ and then from -1×10^{-6} through $-1 \times 10^{-4}\,\text{s}^{-1}$. At $\omega = 1 \times 10^{-4}\,\text{s}^{-1}$ (Fig. 9a), the dipole has a cyclone north of the center and an anticyclone south of it so that the streamfunction phase lags the forcing by $\pi/2$ and is opposite to that expected from steady-state tangential advection of planetary vorticity alone. When the frequency decreases to $1 \times 10^{-5}\,\text{s}^{-1}$ (Fig. 9b), the gyres rotate cyclonically by about $\pi/4$, but the flow across the center rotates $\pi/2$ to straight northward. When $\omega = 1 \times 10^{-6}\,\text{s}^{-1}$ (Fig. 9c) the streamfunction amplitude is largest, and the flow across the center is toward approximately 315°, consistent with the β drift. In subsequent frames, the cyclonic rotation continues (Figs. 9d and 9e), ultimately producing a phase rotation of π when $\omega < -1 \times 10^{-5}\,\text{s}^{-1}$ (Fig. 9f). This gyre orientation also lags the—now oppositely rotating—forcing by $\pi/2$.

In these realizations the Newtonian dissipation time (i.e., time to decrease the amplitude by a factor of e^{-1}) is 16 days. In other calculations, the maximum amplitude of the streamfunction is inversely proportional to the Newtonian dissipation rate. The gyres appear to be hydrodynamically stable because experimentation with different ω and dissipation times of 1–16 days yields no apparent resonance for the imaginary part of the frequency.
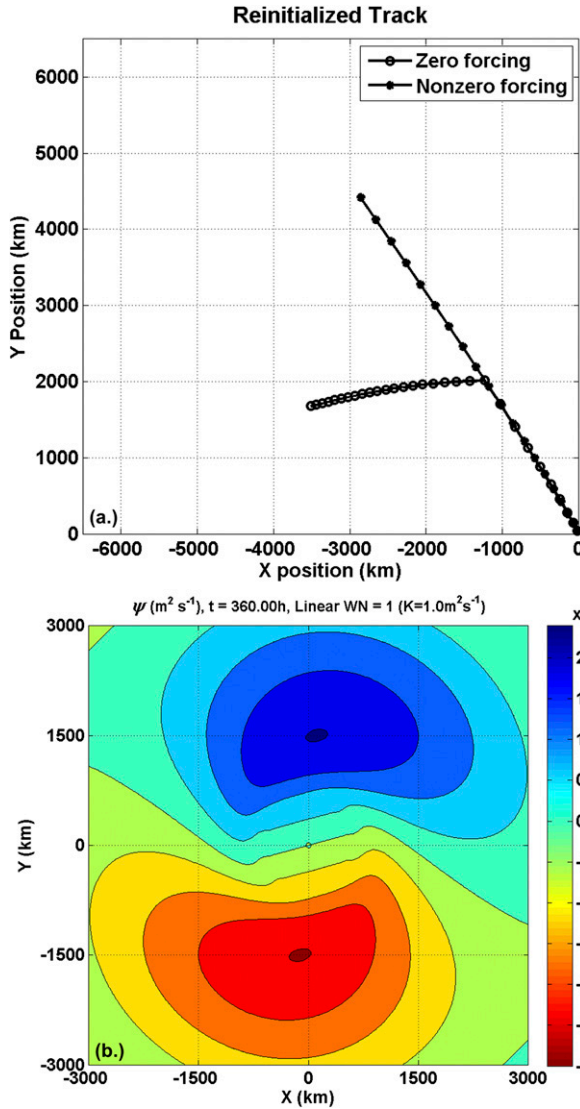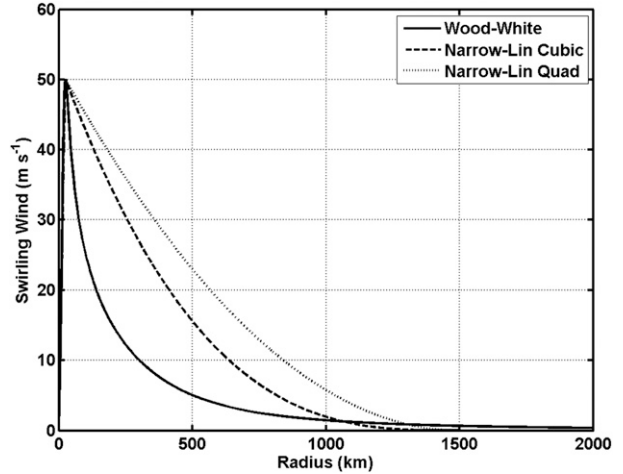
FIG. 12. Three analytical wind profiles: gradient-balanced WW11 (solid, as in Fig. 2), the narrow-transition, linear-quadratic sectionally continuous profile (dotted), and the narrow-transition, linear-cubic profile (dashed). The second and third profiles have identically zero circulation beyond $r = 1500$ km.

7. Linear-model reinitialization

Reinitialization of the linear model replicates another test of the normal-mode hypothesis. Running the linear model for five simulated days produces mature β-gyre asymmetries. Then the resulting β gyres are rotated and scaled and used to initialize the vortex motion on an f plane. If the β gyres are free waves, then the motion should persist and turn at a rate consistent with the frequency identified in the previous section.

In these simulations arbitrary direction and speed are selected. They produce a complex factor used to multiply Ψ_1 to produce an initial asymmetry consistent with the desired motion. In the case shown, the β effect is turned off after simulated day 5. The reinitialization imposes 5 m s^{-1} translation speed toward 270°.

For the remainder of the simulation, the vortex track exhibits slow cyclonic curvature and gradual deceleration (Fig. 11a). By day 10 (5 days after β was turned off), the vortex speed has decreased fairly quickly to 2.5 m s^{-1}, but ultimately, the rate of deceleration slows and levels off, yielding a speed of about 2 m s^{-1} after 10 days of unforced motion (i.e., day 15 of the simulation). The gradual cyclonic curvature and slowing of the motion are consistent with the very low (but nonzero) frequencies and leaking of wave energy to the critical radius where it is symmetrized. The streamfunction field at 360 h (Fig. 11b) illustrates the persistent rotated β-gyre structure. The ventilation flow between the streamfunction gyres is now toward the west-southwest, consistent with their reinitialization and subsequent rotation.

FIG. 11. (a) Track of a vortex moving on a β plane, as in Fig. 4a, and then reinitialized after 120 h by rotating and scaling the β gyres to produce a motion toward 270° at 5 m s^{-1}. (b) Streamfunction 10 days after the reinitialization.

Maximum streamfunction amplitude (Fig. 10) plotted as a function of ω clearly shows a peak response at $\omega = 1 \times 10^{-6} \text{ s}^{-1}$, where the gyre orientation is most like the zero-frequency β gyres of a moving vortex. The amplitude increases as the frequency decreases toward that value, exhibits a sharp maximum, and then decreases at increasingly negative frequencies. The maximum coincides with the phase reversal. The Doppler-shifted frequencies of the β-gyre-like waves allow them to propagate between Ω_{1D} and zero frequency. As in the time-domain model, the waves are confined to a narrow waveguide at a very low, positive, cyclonic frequency.
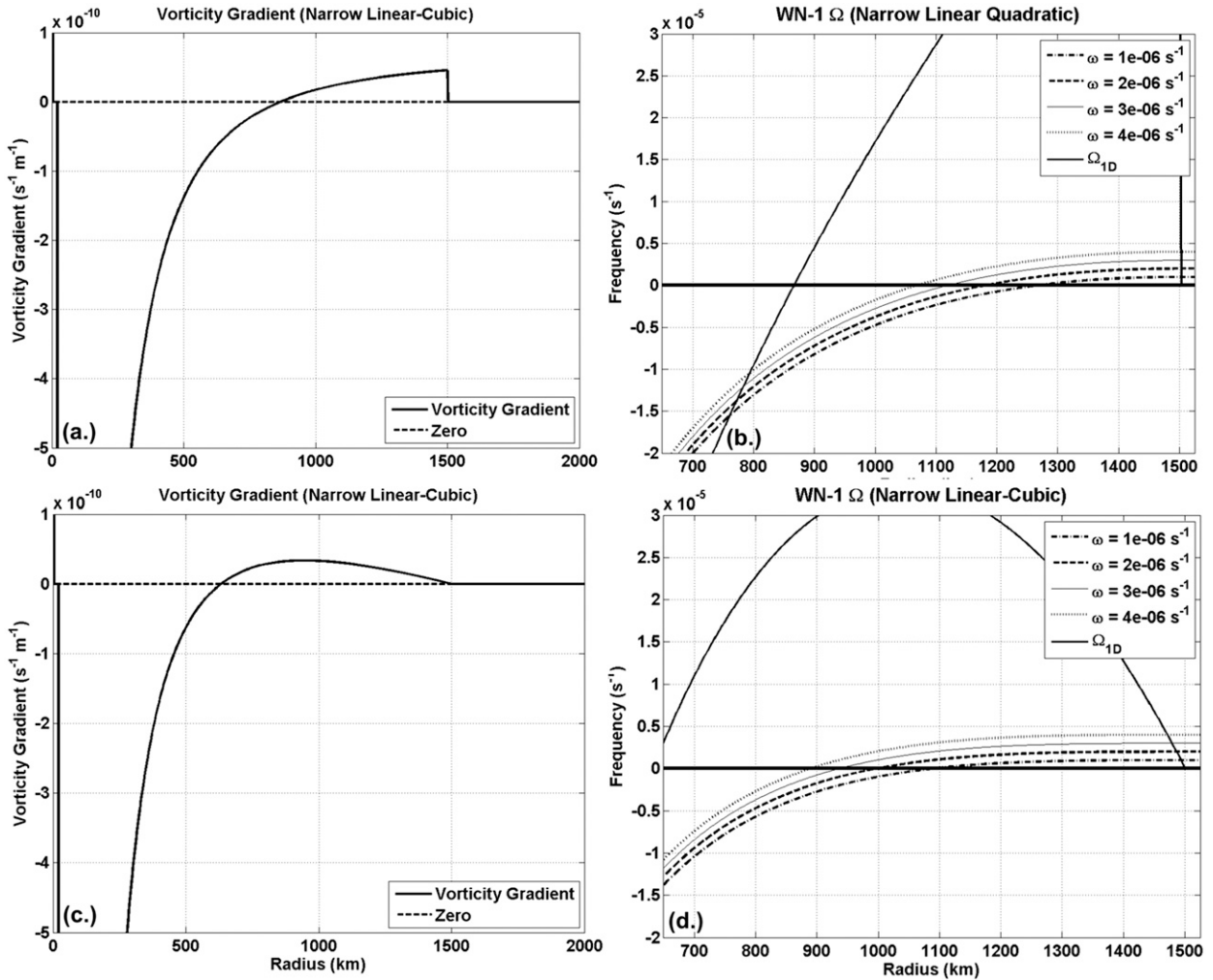
FIG. 13. The outer waveguide for two finitely bounded vortices: (a) radial vorticity gradient for the linear-quadratic profile; (b) Ω_{1D} and selected very low Doppler-shifted frequencies, also for the linear-quadratic profile; and (c),(d) as in (a) and (b), but for the linear-cubic profile.

8. Other profiles

This paper focuses on motion of the gradient wind WW11 vortex on a β plane. We chose that mean vortex because it is both reasonably realistic and fundamentally different from the mean vortices used in MMN, W92, and W94. In this section we compare β-plane simulations using the MMN and WW11 vortices with two model vortices that exhibit the essential features of those used in W92 and W94.

The WW11 vortex is "asymptotically bounded" in the sense that its circulation approaches zero at large radius, but never becomes identically zero. It contrasts with the "unbounded" vortex of MMN in which the vorticity is monotonic and concentrated around the center (e.g., Fig. 3b), such that the circulation becomes constant at large radius.

Two additional vortices examined (Fig. 12) are sectionally continuous, made up of solid rotation near the center, a

narrow quadratic transition across the radius of maximum wind, and a power-law outer wind profile in which the wind goes smoothly to zero at a specified outer radius. Thus, they are "finitely bounded" in the sense that they have identically zero circulation beyond the outer radius. Their piecewise continuous structures are specified by

$$v(r) = v_2 \frac{r}{r_2}, \quad (0 \leq r \leq r_2),$$

$$v(r) = \frac{v_M}{r_M^2}(-4r^2 + 8r_M r - 3r_M^2), \quad (r_2 \leq r \leq r_1),$$

$$v(r) = v_1 \left(\frac{r_9 - r}{r_9 - r_1} \right)^n, \quad (r_1 \leq r \leq r_9),$$

$$v(r) = 0, \quad (r_9 \leq r). \tag{9}$$

The parameters in (9) are radius of maximum wind r_M; maximum wind v_M; radius and wind at the inner

transition, $r_2 < r_M$ and v_2; radius and wind at the outer transition, $r_1 > r_M$, and v_1; the outer bounding radius r_9; and exponent of the outer parabola n. The transition winds and radii are chosen to generate smooth wind profiles. The "linear quadratic" profile uses $n = 2$, and the "linear cubic" profile uses $n = 3$.

Both of these finitely bounded vortices exhibit outer annuli of anticyclonic vorticity and peripheral rings of positive vorticity gradient that support the outer wave-guides. The linear-quadratic profile's (Fig. 13a) positive vorticity gradient extends from about 850 to 1500 km. At the outer boundary, the vorticity gradient jumps to zero discontinuously. As a result, the Ω_{1D} profile exhibits a "shark's fin" shape with the largest value at the discontinuity (Fig. 13b). The waveguide extends from 1050 km to the bounding radius.

The linear-cubic wind profile decreases more quickly outside r_M and is flatter near the bounding radius. As a result, the inner waveguide (Fig. 13c) is narrower, the outer waveguide is wider, and the vorticity gradient goes smoothly to zero at r_9. Positive Ω_{1D} extends from 630- to 1500-km radius and a dense set of very-low-frequency quasimode-like waves can propagate between $r = 900$–1075 and 1500 km (Fig. 13d).

Beta-plane simulations with all four profiles exhibit northwestward tracks (Fig. 14). The MMN profile moved fastest, traveling 8270 km in 240 h, with an average speed of 9.6 m s^{-1}. This speed is over 50% faster than the asymptotic speed originally simulated in MMN because of BND dynamics and much weaker diffusion. It was only slightly faster than the linear-quadratic profile, which travels 7920 km with average speed 9.2 m s^{-1}. Reflection from the peripheral vorticity-gradient jump may explain the faster propagation. Despite its wider waveguide, the linear-cubic profile is significantly slower (6600 km, 7.6 m s^{-1}). Slowest of all was the WW11 profile (5270 km, 6.1 m s^{-1}).

Although the wavenumber-1 streamfunction fields for these simulations are similar, apart from horizontal scale, the vorticity fields after 240 h differ qualitatively. The WW11 vortex exhibits two interlocking trailing spirals (Fig. 15a, also Fig. 5a) that become filamented at the critical radius $r = 500$–800 km and extend outward beyond $r > 2000$ km. They are plausibly described as very-low-frequency vortex Rossby waves, but the dynamics may be more complicated.

The outer region of the MMN vortex (Fig. 15b) exhibits no advection of mean-flow vorticity by the perturbation flow because the mean vortex is irrotational beyond $r = 500$ km. Thus, it cannot support outer vortex Rossby waves. Nonetheless, it does show the same filamentation at slightly smaller radius than the WW11 vortex, with trailing spirals extending to the boundaries
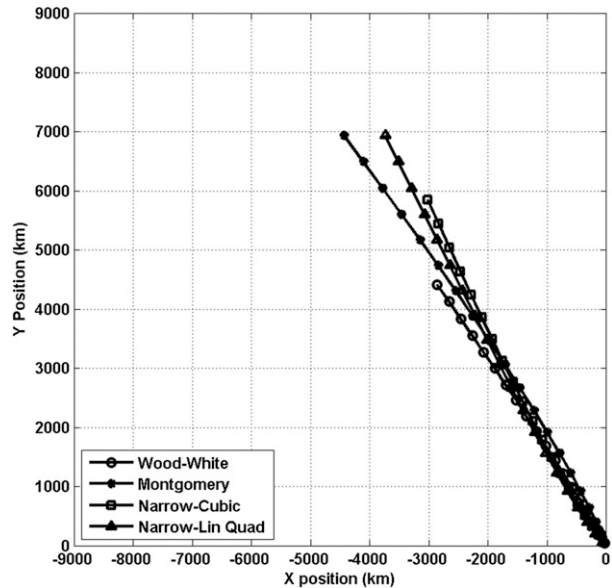

FIG. 14. Comparison among tracks for 240-h simulations of the motions on a β plane of vortices with WW11, MMN, linear-cubic, and linear-quadratic mean-wind profiles.

of the domain. At the more distant end of the domain, the vorticity equation reduces to a balance between the Eulerian derivative of perturbation vorticity and meridional advection of planetary vorticity, resulting in largest amplitude west and east of the center. Closer to the center, azimuthal advection becomes significant so that the spirals wrap around to the southern and northern sides of the center (e.g., Chan and Williams 1987) and ultimately become filamented. Strong forcing due to advection by the irrotational outer vortex accounts for the large amplitude and fast motion.

Both of the finitely bounded vortices exhibit trailing spirals confined to the outer waveguide with filamentation at the critical radius and reflection at the bounding radius. The linear-quadratic profile (Fig. 15c) has a narrower waveguide with maximum vorticity at the outer bounding discontinuity of the mean vorticity gradient. We argue that resonant forcing of these waves, albeit damped by critical radius absorption, explains the rapid propagation even though the β forcing is comparatively weak because the vortex is more compact than the WW11 or MMN profiles.

The linear-cubic vortex (Fig. 15d) has a broader waveguide, 900–1500 km, with maximum vorticity amplitude near its middle and critical radius absorption at its inner boundary. A more diffuse locus of reflection at the waveguide's outer boundary and a somewhat sharper gradient of mean-flow angular velocity near the critical radius render the waveguide leakier, resulting in smaller amplitude and slower propagation.
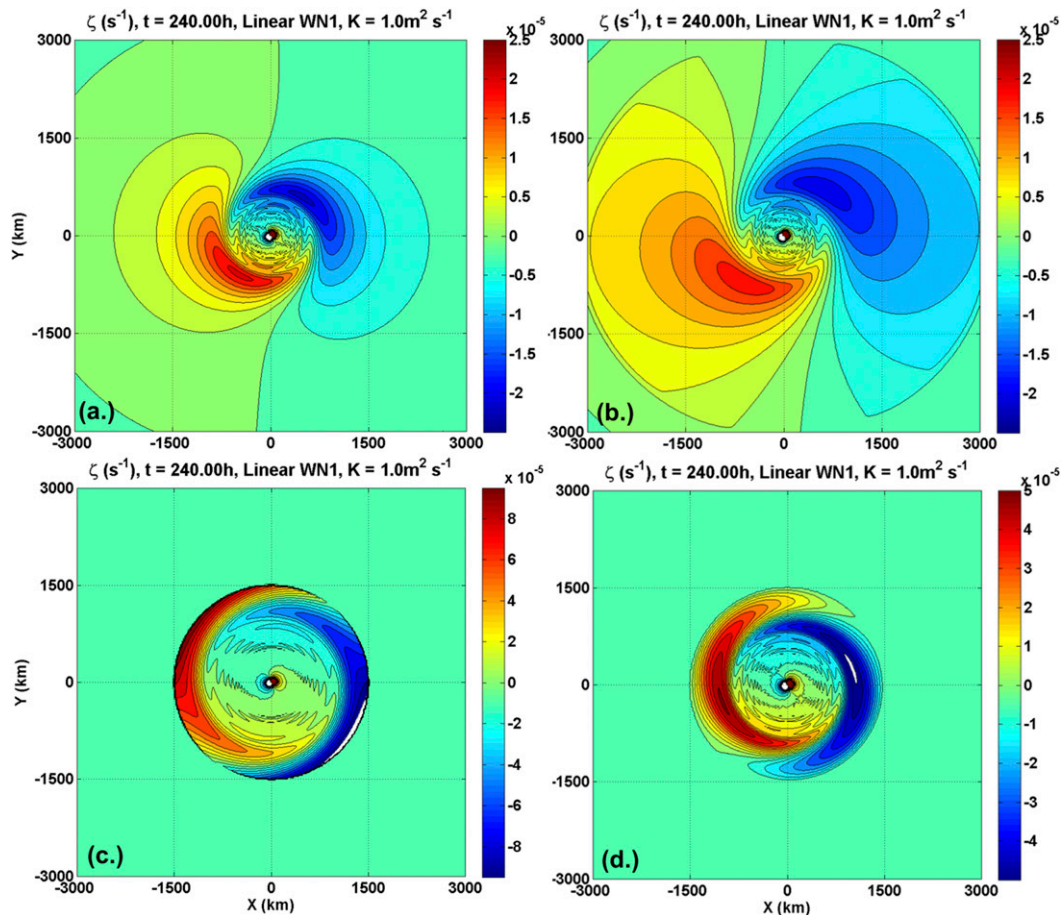
FIG. 15. Comparison among relative vorticity fields after 240 h for (a) WW11, (b) MMN, (c) linear-quadratic, and (d) linear-cubic vortices moving on a β plane.

Tracks of the WW11 (Fig. 16a) and MMN (Fig. 16b) vortices are sensitive to the value of the second-order diffusion constant K. It is much smaller than that used in the earlier studies, ranging from 0.5 through $4 \, m^2 \, s^{-1}$. The MMN vortex is faster for all values. Translation speeds generally accelerate without limit throughout the 240-h simulation when $K \leq 1$ and asymptote when $K \geq 1.5 \, m^2 \, s^{-1}$.

Unlimited acceleration or asymptotic speed was a central discrepancy between these earlier studies. Prognostic variables in both studies were velocity components and geopotential or fluid depth. While both earlier models contained the essential physics of filamentation, the process was less well represented than in the present model where vorticity is the prognostic variable. Use of fourth-order diffusion in MMN resulted in more realistic and stronger dissipative loss at the critical radius that limited the growth of the β gyres and acceleration of the vortex translation. Second-order diffusion in W92 underestimated critical-radius damping so that the radially trapped normal mode could grow resonantly in

the outer waveguide of the finitely bounded mean vortex. The WW11 vortex probably represents an intermediate case. It has an outer waveguide, but the mean radial vorticity gradient is fairly weak, and β advection by the mean flow is strong so that the vorticity spirals are plausibly a superposition of waves trapped in the outer waveguide and nonpropagating vorticity asymmetries.

9. Conclusions

The present barotropic nondivergent, vortex-following model is the simplest framework within which to study rotational dynamics of vortex motion initialized from rest in a quiescent environment on a β plane. The linear results attempt to replicate the vortex-following, linear shallow-water, primitive-equation model (W92) in a completely reformulated MATLAB implementation. This model simulates β gyres with southeast-to-northwest flow between them and a steadily accelerating northwestward
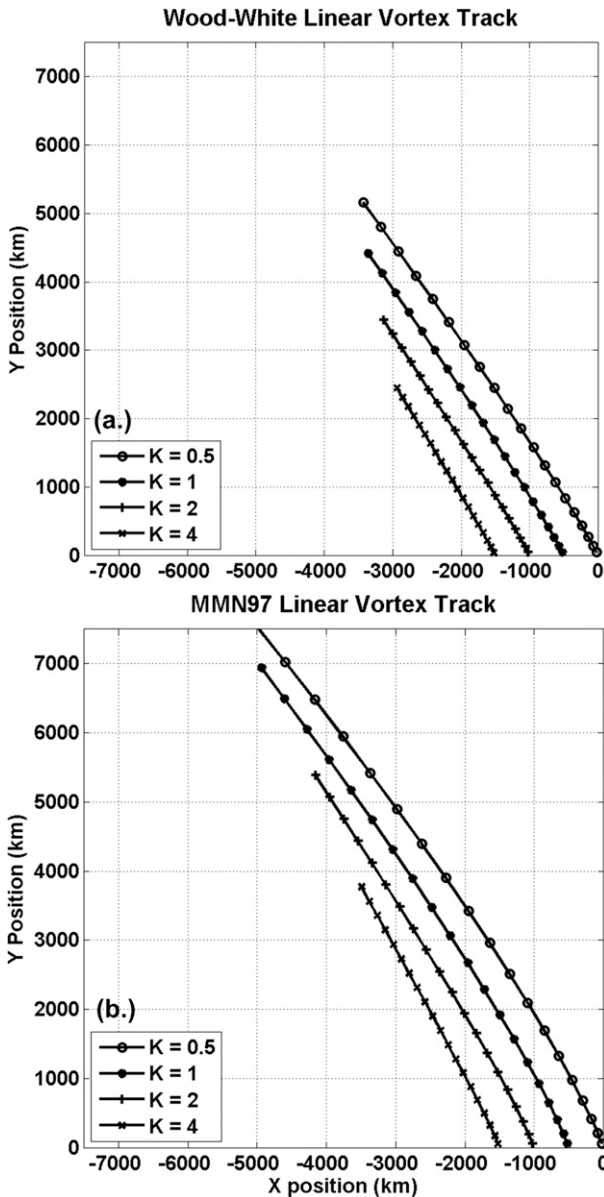
Wood-White Linear Vortex Track

MMN97 Linear Vortex Track

FIG. 16. Comparison between 240-h tracks for (a) WW11 and (b) MMN vortices moving on a β plane with diffusion constants $K = 0.5$–$4\,\mathrm{m^2\,s^{-1}}$.

vorticity, rather than to velocity components and mass variables, increases dissipation near the Rossby wave critical radius.

The analogous nonlinear results also replicate W94 inasmuch as wave–wave interactions limited the vortex translation speed to reasonable values. In addition, isolation of nonlinearly forced anti-β gyres reveals a clear and readily understood mechanism for reduced speed. The nonlinearly excited wavenumber-1 asymmetry has the same structure as the linear β gyres, but opposite polarity. Thus, the flow they induce across the vortex partially cancels the linear southeast-to-northwest flow and so limits the vortex speed. The radial variations of the Doppler-shifted frequencies show that the β gyres behave like a leaky normal mode with a critical radius at the inner edge of the waveguide.

Two additional replications of the earlier normal-mode hypotheses are frequency-domain simulations and reinitialization. In the frequency-domain model, inner boundary conditions on an annular domain suppress the α-gyre asymmetries and the vorticity equation is forced at a specified low frequency. The resulting wavenumber-1 asymmetry at very low cyclonic frequencies has structure and orientation consistent with the β gyres. In reinitialization, the β-effect forcing is turned off at a specified simulated time and the vorticity field is scaled or reoriented. The vortex turns slowly in a cyclonic sense, consistent with the low cyclonic frequencies of free vortex Rossby waves in the outer waveguide. As vorticity leaks inward to the VRW critical radius, the β gyres and motion decay fairly quickly initially and then move slowly before leveling off through the remainder of the simulation.

Replication of the unlimited linear acceleration and asymptotic nonlinear acceleration for small diffusion supports earlier results. The existence of the outer waveguide is the key to understanding the β gyres as free waves. It permits propagation only in a narrow very-low-frequency passband in bounded vortices. The wavenumber-1 asymmetry is not a single normal mode in a traditional sense but resembles a quasimode, a narrow continuum of waves that are slowly damped through axisymmetrization at their critical radii.

As idealized as these simulations are, they suggest that operational vortex bogusing with carefully designed wavenumber-1, and perhaps wavenumber-2, asymmetries on finitely bounded vortices may be a good way to avoid initialization transients and adjust initial vortex motion. Baroclinic mean vortices and sparse observations make observational verification challenging. Nonetheless, the basic structures of the beta gyres and their influence on motion have long-standing observational support (Holland 1984).

motion. These waves' properties are consistent with vortex Rossby waves that propagate downstream on the reversed mean-flow vorticity gradient at the periphery of the asymptotically bounded mean vortex. For small diffusion ($K < 1\,\mathrm{m^2\,s^{-1}}$), the vortex accelerates throughout the simulation. For larger values, it asymptotically approaches an unphysically fast speed, consistent with previously published AB results. These values of K are more than an order of magnitude smaller than those used previously because somewhat finer resolution and application of the diffusion to

REFERENCES

Chan, J. C. L., 2005: The physics of tropical cyclone motion. *Annu. Rev. Fluid Mech.*, **37**, 99–128, doi:10.1146/annurev.fluid.37.061903.175702.

——, and R. T. Williams, 1987: Analytical and numerical studies of the beta-effect in tropical cyclone motion. Part I: Zero mean flow. *J. Atmos. Sci.*, **44**, 1257–1265, doi:10.1175/1520-0469(1987)044<1257:AANSOT>2.0.CO;2.

Cotto, A., 2012: Intermittently forced vortex Rossby waves. M.S. thesis, Dept. of Earth and Environment, Florida International University, 81 pp. [Available online at http://digitalcommons.fiu.edu/etd/553.]

——, I. Gonzalez III, and H. E. Willoughby, 2015: Synthesis of vortex Rossby waves. Part I: Episodically forced waves in the inner waveguide. *J. Atmos. Sci.*, **72**, 3940–3957, doi:10.1175/JAS-D-15-0004.1.

Gonzalez, I., III, 2014: Linear and nonlinear motion of a barotropic vortex. M.S. thesis, Dept. of Geosciences, Florida International University, 44 pp. [Available online at http://digitalcommons.fiu.edu/etd/1196.]

Holland, G. J., 1983: Tropical cyclone motion: Environmental interaction plus a beta effect. *J. Atmos. Sci.*, **40**, 328–342, doi:10.1175/1520-0469(1983)040<0328:TCMEIP>2.0.CO;2.

——, 1984: Tropical cyclone motion: A comparison of theory and observation. *J. Atmos. Sci.*, **41**, 68–75, doi:10.1175/1520-0469(1984)041<0068:TCMACO>2.0.CO;2.

Li, X., and B. Wang, 1994: Barotropic dynamics of the beta gyres and beta drift. *J. Atmos. Sci.*, **51**, 746–756, doi:10.1175/1520-0469(1994)051<0746:BDOTBG>2.0.CO;2.

Lindzen, R. S., and H. L. Kuo, 1969: A reliable method for the numerical integration of a large class of ordinary and partial differential equations. *Mon. Wea. Rev.*, **97**, 732–734, doi:10.1175/1520-0493(1969)097<0732:ARMFTN>2.3.CO;2.

——, and K. K. Tung, 1978: Wave overreflection and shear instability. *J. Atmos. Sci.*, **35**, 1626–1632, doi:10.1175/1520-0469(1978)035<1626:WOASI>2.0.CO;2.

——, and J. W. Baker, 1985: Instability and overreflection in stably stratified shear flows. *J. Fluid Mech.*, **151**, 189–217, doi:10.1017/S0022112085000921.

MacDonald, N. J., 1968: The evidence for the existence of Rossby-like waves in the hurricane vortex. *Tellus*, **20**, 138–150, doi:10.1111/j.2153-3490.1968.tb00358.x.

Montgomery, M. T., and L. J. Shapiro, 1992: A three-dimensional balance theory for rapidly rotating vortices. *J. Atmos. Sci.*, **50**, 3322–3335, doi:10.1175/1520-0469(1993)050<3322:ATDBTF>2.0.CO;2.

——, and R. J. Kallenbach, 1997: A theory for vortex Rossby waves and its application to spiral bands and intensity changes in hurricanes. *Quart. J. Roy. Meteor. Soc.*, **123**, 435–465, doi:10.1002/qj.49712353810.

——, D. J. Möller, and C. T. Nicklas, 1999: Linear and nonlinear vortex motion in an asymmetric balance shallow water model. *J. Atmos. Sci.*, **56**, 749–768, doi:10.1175/1520-0469(1999)056<0749:LANVMI>2.0.CO;2.

Ritchie, E. A., and W. M. Frank, 2007: Interactions between simulated tropical cyclone and an environment with a variable Coriolis parameter. *Mon. Wea. Rev.*, **135**, 1889–1905, doi:10.1175/MWR3359.1.

Rossby, C. G., 1948: On displacements and intensity changes of atmospheric vortices. *J. Mar. Res.*, **7**, 175–187.

Schecter, D. A., and M. T. Montgomery, 2003: On the symmetrization rate of an intense geophysical vortex. *Dyn. Atmos. Oceans*, **37**, 55–88, doi:10.1016/S0377-0265(03)00015-0.

——, and ——, 2004: Damping and pumping of a vortex Rossby wave in a monotonic cyclone: Critical-layer stirring versus inertia-buoyancy wave emission. *Phys. Fluids*, **16**, 1334–1348, doi:10.1063/1.1651485.

——, H. E. Dubin, A. C. Cass, C. F. Driscoll, I. M. Lansky, and T. M. O'Neil, 2000: Inviscid damping of asymmetries on a two-dimensional vortex. *Phys. Fluids*, **12**, 2397–2412, doi:10.1063/1.1289505.

Willoughby, H. E., 1988: Linear motion of a shallow-water, barotropic vortex. *J. Atmos. Sci.*, **45**, 1906–1928, doi:10.1175/1520-0469(1988)045<1906:LMOASW>2.0.CO;2.

——, 1992: Linear motion of a shallow-water barotropic vortex as an initial-value problem. *J. Atmos. Sci.*, **49**, 2015–2031, doi:10.1175/1520-0469(1992)049<2015:LMOASW>2.0.CO;2.

——, 1994: Nonlinear motion of a shallow-water barotropic vortex. *J. Atmos. Sci.*, **51**, 3722–3744, doi:10.1175/1520-0469(1994)051<3722:NMOASW>2.0.CO;2.

——, 2011: The golden radius in balanced atmospheric flows. *Mon. Wea. Rev.*, **139**, 1164–1168, doi:10.1175/2010MWR3579.1.

Wood, V. T., and L. W. White, 2011: A new parametric model of vortex tangential-wind profiles: Development, testing, and verification. *J. Atmos. Sci.*, **68**, 990–1006, doi:10.1175/2011JAS3588.1.